

Hyperspectral and Multispectral Image Fusion Using the Conditional Denoising Diffusion Probabilistic Model

Shuaikai Shi, *Student Member, IEEE*, Lijun Zhang, Jie Chen, *Senior Member, IEEE*

Abstract—Hyperspectral images (HSI) have a large amount of spectral information reflecting the characteristics of matter, while their spatial resolution is low due to the limitations of imaging technology. Complementary to this are multispectral images (MSI), e.g., RGB images, with high spatial resolution but insufficient spectral bands. Hyperspectral and multispectral image fusion is a technique for acquiring ideal images that have both high spatial and high spectral resolution cost-effectively. Many existing HSI and MSI fusion algorithms rely on known imaging degradation models, which are often not available in practice. In this paper, we propose a deep fusion method based on the conditional denoising diffusion probabilistic model, called DDPM-Fus. Specifically, the DDPM-Fus contains the forward diffusion process which gradually adds Gaussian noise to the high spatial resolution HSI (HrHSI) and another reverse denoising process which learns to predict the desired HrHSI from its noisy version conditioning on the corresponding high spatial resolution MSI (HrMSI) and low spatial resolution HSI (LrHSI). Once the training is completed, the proposed DDPM-Fus implements the reverse process on the test HrMSI and LrHSI to generate the fused HrHSI. Experiments conducted on one indoor and two remote sensing datasets show the superiority of the proposed model when compared with other advanced deep learning-based fusion methods. The codes of this work will be open-sourced at this address: <https://github.com/shuaikaishi/DDPMFus> for reproducibility.

Index Terms—Image fusion, hyperspectral image, multispectral image, probabilistic model, super-resolution.

I. INTRODUCTION

SPECTRAL imaging allows for the simultaneous capture of both spatial and spectral information of a scene, providing light reflectance information beyond human perception. Benefiting from abundant spectral features, this technique has been used in a wide-range of applications, including face recognition [1], object detection [2], remote sensing [3], agriculture [4], etc. However, the HSI typically has lower spatial resolution than the RGB images due to the larger instantaneous field of view (IFOV) [5]. In practice, it is only possible to capture either HrMSI or LrHSI in a single imaging shot. This has a significant impact on the accuracy and reliability of the analysis results obtained from the captured data. Fortunately, HSI-MSI fusion [6] can fuse a pair of degraded HrMSI and

LrHSI to produce the desired HrHSI. This fusion technique overcomes the limitations of acquiring HrHSI in a single shot and enables a wider range of applications.

A. Motivation

Classical HSI-MSI fusion approaches generally assume the parameters of the observation model, i.e., point spread function (PSF) in the spatial degradation and spectral response function (SRF) in the spectral degradation, are known. However, in practice, the degradation processes are complex and the parameters may be difficult or even impossible to accurately determine [7]. Therefore, the performance of such conventional models is limited when the degradation models mismatch the actual system.

Deep learning-based methods have already been introduced to address the HSI-MSI fusion problem, restore the spatial and spectral details of HrHSI and yield desired results. These models use deep neural networks, such as convolutional neural networks (CNNs) and Transformer [8], to learn the mapping from (HrMSI, LrHSI) pairs to HrHSI. Thanks to the extensive expressive ability of neural networks, these models can produce high-definition HrHSI. However, on one hand, the most of existing fusion networks fuse the input degraded images to the output HrHSI at one step, which can be further improved by incorporating multiple iterative models. On the other hand, the regression-based methods may have restricted practical generalization ability on the new test data caused by overfitting. Fortunately, this problem can be alleviated by introducing generative models, such as the recently proposed diffusion model [9]. Inspired by these two points, we propose a novel multi-stage HSI-MSI fusion model.

B. Methodology Overview and Contributions

Recently, the denoising diffusion probabilistic model (DDPM) [9] has been attracted great attention in the community of deep generative models and used for various generative tasks, e.g., image generation [10] and audio synthesis [11]. Furthermore, the DDPM with extra inputs can be used for the conditional generation, such as image superresolution [12], text-to-image generation [13] and image editing [14], concluding inpainting, colorization and uncropping.

The DDPM learns to produce a clean output from its noisy version via multiple denoising steps. Specifically, the DDPM contains two processes, namely, the forward diffusion process and the reverse denoising process. In the training phase, the

Shuaikai Shi, Lijun Zhang and Jie Chen are with the Center of Intelligent Acoustics and Immersive Communications, School of Marine Science and Technology, Northwestern Polytechnical University, Xi'an 710072, China, and also with the Key Laboratory of Ocean Acoustics and Sensing, Ministry of Industry and Information Technology, Xi'an 710072, China (e-mail: shuaikai_shi@mail.nwpu.edu.cn; zhanglj7385@nwpu.edu.cn; dr.jie.chen@ieee.org).

diffusion process adds independent Gaussian noise to the clean sample multiple times resulting in the final output tending towards a standard Gaussian distribution. Then the denoising process, constructed by a deep neural network, learns the reverse mapping from noisy data to the original clean data. Once training is complete, the DDPM can generate new samples via implementing the denoising process with Gaussian noise inputs. Moreover, the conditional DDPM introduce an extra input in the reverse denoising process to guide the model outputs samples related to this input, e.g., produce a high resolution image corresponding to the blur input rather than output an another unrelated image. Inspired by the conditional DDPM, we propose an HSI-MSI fusion model, called DDPM-Fus, using the HrMSI and LrHSI as conditional inputs. The proposed DDPM-Fus fuses the HrMSI and LrHSI by a U-net architecture and predicts the added Gaussian noises to recover the spatial details and spectral signatures of the desired HrHSI.

The main contributions of this work are summarized as:

- 1) We propose a novel HSI-MSI fusion model by adapting the denoising diffusion probabilistic model to HSI generation with conditional inputs. Our proposed model outperforms commonly used discriminative models and shows great potential for recovering HrHSI.
- 2) The proposed model, DDPM-Fus, produces the fused results by multiple iterative denoising that is distinguished it from the general deep learning-based single-step fusion models.
- 3) We demonstrate the fusion on three public hyperspectral data and experiment results show the superiority of the proposed conditional generative model compared to the regression-based fusion approaches.

The rest of this paper is organized as follows. The related work is reviewed in Section II. Section III presents the proposed DDPM-Fus. The fusion experiments conducted on three HSI datasets are demonstrated in Section IV to show the effectiveness of DDPM-Fus. Section V concludes this paper and provides a discussion.

II. RELATED WORK

HSI-MSI fusion has been seen as an effective tool to obtain the desired HrHSI. In our text, the fusion approaches are divided into two types, namely, conventional unsupervised methods, which often use the observed model as priors, and advanced supervised deep learning-based models, which usually rely on ground truth HrHSI data for training.

A. Unsupervised HSI-MSI Fusion

Pansharpening algorithms [15] have been extended to the HSI-MSI fusion. Gram-Schmidt adaptive (GSA) [16] is a representative pansharpening algorithm based on component substitution, which uses Gram-Schmidt transformation to separate the spatial component of the LrHSI that needs to be substituted by the HrMSI. The generalized Laplacian pyramid-based hyper-sharpening (GLP-HS) [17] adapts another class of pansharpening methods to HSI-MSI fusion that uses the pyramidal decompositions to obtain the high spatial resolution details in the scene. Then the spatial details are injected into

the LrHSI to obtain the desired HrHSI. Pansharpening-based fusion methods implement fast and independent of observation model, however, these methods may produce HrHSI with coarse spatial details and spectral distortion due to the simplistic model design.

Subspace representation-based fusion methods usually use a spectral dictionary to represent all spectral signatures of the HrHSI and then obtain the corresponding coefficients by optimizing an objective function. Coupled non-negative matrix factorization (CNMF) [18] embeds the linear mixing model (LMM) into the fusion problem and then endmembers of LrHSI are multiplied by abundances of HrMSI to obtain the fused result. Some constraints are often used to ensure the sparsity of the coefficients and the smoothness of the desired images. Hyperspectral superresolution (HySure) [19] encourages the smoothness of HrHSI using the total variation (TV) regularizers on each band. A non-negative structured sparse representation (NSSR) [20] uses the clustering method to promote spectral homogeneity. The tensor representation is also applied to HSI-MSI fusion. The coupled sparse tensor factorization (CSTF) [21] directly represents the HSI cube by the Tucker decomposition and constrains the sparsity of the core tensor. While subspace representation-based fusion methods can get superior performance over sharpening-based algorithms, the fact that most of these methods use a linear representation that limits their use of them.

An alternative to hand-tuning the regularization parameters is to introduce a neural network to learn prior knowledge in the HrHSI. An unsupervised sparse Dirichlet-Net (uSDN) [22] iteratively learns the shared features of abundances in the LrHSI and HrHSI. A variational autoencoder-like probabilistic generative model (NVPGM) [23] extends uSDN that global training of the model parameters. Guide deep decoder (GDD) [24] learns to produce the desired HSI from noise based on the deep image prior [25]. It degrades HrHSI using an observation model and then minimize the errors between outputs and input images, LrHSI and HrMSI. These unsupervised deep fusion models can produce more accurate results, however, these methods usually assume the observation model is known, resulting in a limitation of their practical use.

B. Supervised HSI-MSI Fusion

Recently, deep learning-based supervised methods have been introduced to HSI-MSI fusion [26]. Benefiting from the expressive capacity of neural networks, these models learn the mapping from a number of paired LrHSI and HrMSI to the ground-truth images HrHSI in an end-to-end manner. Once the training is complete, these fusion models have the generalization ability to fuse other degraded image pairs to the desired HrHSI. Most deep learning-based methods concentrate on exploring the expressive network modules to extract the high spatial resolution information and precision spectral signatures, and then fuse them into output images. The deep pansharpening network (PANnet) [27] with CNNs and the residual block was proposed to fuse a panchromatic image and a corresponding MSI. Wang *et al.* [28] introduced a deep prior to HSI super-resolution, automatically learning the spatial-spectral priors in the scene. Hu *et al.* [29] designed a deep

TABLE I
THE PROPERTIES OF REPRESENTATIVE FUSION METHODS.

Category	Method	Ground truth	PSF	SRF
Pansharpening-based	GSA [16]	✗	✗	✗
	GLP-HS [17]		✗	✗
Subspace-based	HySure [19]	✗	✗	✗
	CNMF [18]		✓	✓
	CSTF [21]		✓	✓
	NSSR [20]		✓	✓
	uSDN [22]		✗	✓
Unsupervised deep learning-based	NVPGM [23]	✗	✗	✓
	GDD [24]		✓	✓
	PANnet [27]		✗	✗
Supervised deep learning-based	HSRnet [29]	✓	✗	✗
	SSRnet [30]		✗	✗
	MHF-net [31]		✗	✗
	EDBIN [32]		✗	✗
	DDPM-Fus (ous)		✗	✗
			✗	✗

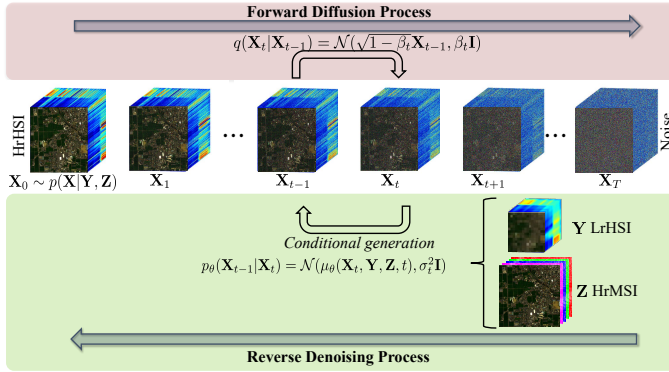


Fig. 1. Framework of the proposed DDPM-Fus, including the forward process and the reverse process. In the forward diffusion process, Gaussian noise is gradually added to HrHSI \mathbf{X}_0 over T time steps. In the reverse denoising process, the neural network $\mu_\theta(\cdot)$ learns to recover the spatial details and spectral signatures of the desired HrHSI by implementing denoising progressively conditioned on two degraded images, \mathbf{Y} and \mathbf{Z} .

convolutional network with the spatial and spectral attention mechanisms to perform the fusion task, called HSRnet. In addition to the one-stage fusion methods mentioned above, multi-stage models are expected to achieve better performance. Zhang *et al.* [30] proposed a three-stage network consisting of preliminary fusion, spatial and spectral refinement, namely SSRnet. Xie *et al.* [31] proposed a physically meaningful HSI-MSI fusion network (MHF-net) which progressively recover the HrHSI through K -stage networks. Wang *et al.* [32] proposed an iterative fusion method to estimate both the observation model and fusion process, namely enhanced deep blind hyperspectral image fusion network (EDBIN). Rather than using known PSF and SRF as in the unsupervised methods, the deep supervised fusion models leverage the high capacity of deep neural networks to restore the HrHSI and achieve state-of-the-art performance. These fusion networks are independent of the observation model, showing promising potential for application in practice. In summary, the properties of several representative fusion methods are shown in Table I.

III. THE PROPOSED DDPM-FUS MODEL

In this section, we present the proposed DDPM-Fus, including the problem formulation, forward and backward processes, objective function, optimization and fast fusion strategy.

A. Problem Formulation

The goal of HSI-MSI fusion is to obtain an HrHSI, $\mathcal{X} \in \mathbb{R}^{L \times W \times H}$, benefiting simultaneously from spatial details of the HrMSI, $\mathcal{Z} \in \mathbb{R}^{l \times W \times H}$, and spectral signatures of the LrHSI, $\mathcal{Y} \in \mathbb{R}^{L \times w \times h}$, where $\{L, W, H\}$ and $\{l, w, h\}$ denote the channels, widths and heights of high-resolution and low-resolution image cubes, respectively. It is generally accepted that, $w \ll W, h \ll H$ and $l \ll L$, thus it is nontrivial to perform the image fusion with strong spatial and spectral resolution differences. The following linear observation model is adopted by most of the fusion literature [20], [21]:

$$\begin{aligned} \mathbf{Y} &= \mathbf{XBS} + \mathbf{N}_y, \\ \mathbf{Z} &= \mathbf{RX} + \mathbf{N}_z, \end{aligned} \quad (1)$$

where $\mathbf{X} \in \mathbb{R}^{L \times W \times H}$, $\mathbf{Y} \in \mathbb{R}^{L \times w \times h}$ and $\mathbf{Z} \in \mathbb{R}^{l \times W \times H}$ are 2D matrices unfolding the corresponding 3D tensors of HrHSI, LrHSI and HrMSI, respectively. $\mathbf{B} \in \mathbb{R}^{W \times H \times W \times H}$ is the blurring matrix constructed by the PSF kernel. $\mathbf{S} \in \mathbb{R}^{W \times H \times w \times h}$ represents the spatial downsampling operator which is used combined with the blurring matrix to formulate the spatial degradation process. $\mathbf{R} \in \mathbb{R}^{l \times L}$, the SRF matrix, denotes the spectral merging process. \mathbf{N}_y and \mathbf{N}_z are two Gaussian noise matrices, which are independent of the image data.

The objective is recovering \mathbf{X} with observations \mathbf{Y}, \mathbf{Z} . In the first class of fusion methods, conventional unsupervised model, \mathbf{B}, \mathbf{S} and \mathbf{R} are often assumed as priors. While in the second class of fusion methods, supervised deep learning-based models, several HrHSI are known as the ground truths for the training of fusion networks. Once the training is complete, these models perform the fusion process in other new observation pairs, \mathbf{Y} and \mathbf{Z} . Our proposed DDPM-Fus is belonging to the second class methods. We see the HSI-MSI fusion problem as modeling the conditional probabilistic distribution $p(\mathbf{X}|\mathbf{Y}, \mathbf{Z})$. Then one can obtain the desired HrHSI by sampling from this distribution. Inspired by the advanced denoising diffusion generative model [9], we build two processes below to learn the above conditional distribution.

B. Forward Diffusion Process

Following DDPM [9], we use a Markovian chain of length T with the Gaussian diffusion kernel adding noise to the HrHSI \mathbf{X} .

$$q(\mathbf{X}_t|\mathbf{X}_{t-1}) = \mathcal{N}(\sqrt{1-\beta_t}\mathbf{X}_{t-1}, \beta_t\mathbf{I}), \quad (2)$$

where $t \in \{1, 2, \dots, T\}$, $\mathbf{X}_0 = \mathbf{X}$ is the ground truth image, \mathbf{X}_T is the noisy image at when the end of the forward process, $\beta_t \in \{\beta_1, \beta_2, \dots, \beta_T\}$ is a sequence of hyperparameters representing the variance of Gaussian noise and \mathbf{I} is the identity matrix.

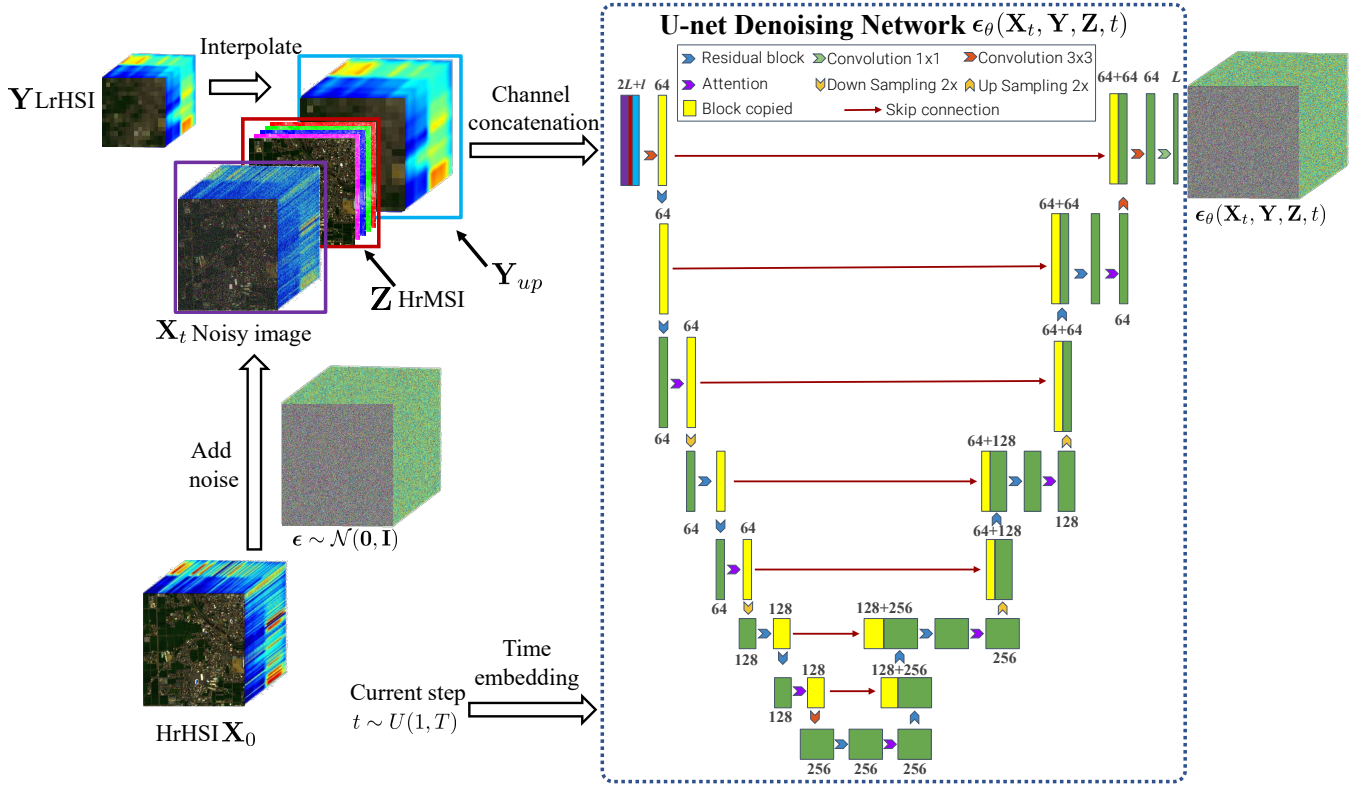


Fig. 2. Structure of the denoising network $\epsilon_\theta(\mathbf{X}_t, \mathbf{Y}, \mathbf{Z}, t)$. In each training time step t , we first obtain \mathbf{X}_t by adding Gaussian noise to HrHSI \mathbf{X}_0 and interpolate LrHSI \mathbf{Y} to the same spatial resolution of HrMSI \mathbf{Z} . Then, \mathbf{X}_t , \mathbf{Z} and \mathbf{Y}_{up} will be used as network inputs after the channel dimensions are concatenated. The current step t will be input to each residual block in the network in the form of a time embedding. In the U-net denoising network, there are a series of convolutional residual blocks, skip connections and attention modules. Last, the network predicts the noise that we add before.

Due to the property of Gaussian distribution, one can directly obtain the output of each diffusion step by

$$q(\mathbf{X}_t|\mathbf{X}_0) = \mathcal{N}(\sqrt{\bar{\alpha}_t}\mathbf{X}_0, \sqrt{1-\bar{\alpha}_t}\mathbf{I}) \quad (3)$$

$$\text{or } \mathbf{X}_t = \sqrt{\bar{\alpha}_t}\mathbf{X}_0 + \sqrt{1-\bar{\alpha}_t}\boldsymbol{\epsilon}, \quad (4)$$

where $\bar{\alpha}_t = \prod_{s=1}^t (1 - \beta_s)$ and $\boldsymbol{\epsilon} \sim \mathcal{N}(\mathbf{0}, \mathbf{I})$. Note that when $T \rightarrow \infty$, $q(\mathbf{X}_\infty) = \mathcal{N}(\mathbf{0}, \mathbf{I})$.

The forward diffusion is shown at the top of Fig. 1.

C. Reverse Denoising Process

After the forward diffusion process, we use the reverse denoising process to recover the HrHSI from the noise input and the pairs of LrHSI and HrMSI. Specifically, the reverse process maps from the standard Gaussian noise to the HrHSI \mathbf{X} and we assume the inverse of the above forward diffusion kernel (2) is another Gaussian as

$$p_\theta(\mathbf{X}_{t-1}|\mathbf{X}_t) = \mathcal{N}(\mu_\theta(\mathbf{X}_t, \mathbf{Y}, \mathbf{Z}, t), \sigma_t^2 \mathbf{I}), \quad (5)$$

where $\mu_\theta(\cdot)$ is constructed by a deep neural network parameterized by θ and $\sigma_t^2 \in \{\sigma_1^2, \sigma_2^2, \dots, \sigma_T^2\}$ is a sequence of hyperparameters, which will be given in the Sec. III-D.

D. Objective Function

In this subsection, we present the objective function of the proposed DDPM-Fus. The evidence lower bound (ELBO) of the log-likelihood is

$$\mathcal{L}(\theta) = - \sum_{t=1}^T \text{KL}(q(\mathbf{X}_{t-1}|\mathbf{X}_t, \mathbf{X}_0) || p_\theta(\mathbf{X}_{t-1}|\mathbf{X}_t)), \quad (6)$$

where $\text{KL}(\cdot || \cdot)$ denotes the Kullback-Leibler divergence between two distributions. The detailed derivation of (6) will be given in the APPENDIX. $q(\mathbf{X}_{t-1}|\mathbf{X}_t, \mathbf{X}_0)$ is the posterior distribution which can be deduced to

$$\begin{aligned} q(\mathbf{X}_{t-1}|\mathbf{X}_t, \mathbf{X}_0) &\propto q(\mathbf{X}_t|\mathbf{X}_{t-1}, \mathbf{X}_0)q(\mathbf{X}_{t-1}|\mathbf{X}_0) \\ &= q(\mathbf{X}_t|\mathbf{X}_{t-1})q(\mathbf{X}_{t-1}|\mathbf{X}_0). \end{aligned} \quad (7)$$

Since the conditional distribution (2) and the prior distribution (3) here are both Gaussian, the posterior distribution is also Gaussian due to the self-conjugate nature of the Gaussian distribution [33]. Thus the above distribution (7) is

$$q(\mathbf{X}_{t-1}|\mathbf{X}_t, \mathbf{X}_0) = \mathcal{N}(\tilde{\mu}_t(\mathbf{X}_t, \mathbf{X}_0), \tilde{\beta}_t \mathbf{I}), \quad (8)$$

where

$$\tilde{\mu}_t(\mathbf{X}_t, \mathbf{X}_0) = \frac{\sqrt{1-\beta_t}(1-\bar{\alpha}_{t-1})}{1-\bar{\alpha}_t} \mathbf{X}_t + \frac{\sqrt{\bar{\alpha}_{t-1}}\beta_t}{1-\bar{\alpha}_t} \mathbf{X}_0, \quad (9)$$

$$\tilde{\beta}_t = \frac{1-\bar{\alpha}_{t-1}}{1-\bar{\alpha}_t} \beta_t. \quad (10)$$

Algorithm 1: Training algorithm of DDPM-Fus

Input: paired training data: $(\mathbf{Y}, \mathbf{Z}, \mathbf{X}_0)$;
hyperparameter sequence: $\{\beta_1, \beta_2, \dots, \beta_T\}$;

- 1 Initialize θ randomly;
- 2 **repeat**
- 3 $\epsilon \sim \mathcal{N}(\mathbf{0}, \mathbf{I})$;
- 4 $t \sim U(1, T)$;
- 5 Compute the noisy image by (4):
 $\mathbf{X}_t = \sqrt{\bar{\alpha}_t} \mathbf{X}_0 + \sqrt{1 - \bar{\alpha}_t} \epsilon$
- 6 Compute the gradient of (15) w.r.t. θ :
 $\nabla_{\theta} \|\epsilon - \epsilon_{\theta}(\mathbf{X}_t, \mathbf{Y}, \mathbf{Z}, t)\|$;
- 7 Update θ via Adam optimizer [34].
- 8 **until training phase end**;

The KL divergence in the ELBO (6) is tractable because all distributions disturbed here are independent Gaussian. Thus the KL divergence at one-time step can be written by

$$\begin{aligned} \mathcal{L}_t(\theta) &= -\text{KL}(q(\mathbf{X}_{t-1}|\mathbf{X}_t, \mathbf{X}_0) \| p_{\theta}(\mathbf{X}_{t-1}|\mathbf{X}_t, \mathbf{Y}, \mathbf{Z})) \\ &= -\frac{1}{2\sigma_t^2} \|\tilde{\mu}_t(\mathbf{X}_t, \mathbf{X}_0) - \mu_{\theta}(\mathbf{X}_t, \mathbf{Y}, \mathbf{Z}, t)\|_F^2 + C, \end{aligned} \quad (11)$$

where C is a constant independent of θ including some untrainable parameters. Following [9], we can use the relationship (4) eliminating \mathbf{X}_0 in (9) as

$$\tilde{\mu}_t(\mathbf{X}_t, \mathbf{X}_0) = \frac{1}{\sqrt{1 - \beta_t}} \left(\mathbf{X}_t - \frac{\beta_t}{\sqrt{1 - \bar{\alpha}_t}} \epsilon \right). \quad (12)$$

Meanwhile, the prediction of the neural network $\mu_{\theta}(\mathbf{X}_t, \mathbf{Y}, \mathbf{Z}, t)$ can be written as the same form

$$\begin{aligned} \mu_{\theta}(\mathbf{X}_t, \mathbf{Y}, \mathbf{Z}, t) \\ = \frac{1}{\sqrt{1 - \beta_t}} \left(\mathbf{X}_t - \frac{\beta_t}{\sqrt{1 - \bar{\alpha}_t}} \epsilon_{\theta}(\mathbf{X}_t, \mathbf{Y}, \mathbf{Z}, t) \right). \end{aligned} \quad (13)$$

where $\epsilon_{\theta}(\cdot)$ is another form of $\mu_{\theta}(\cdot)$, which predicts the noise added in the forward process and will be introduced in the next subsection.

Thus the KL divergence (11) can be further simplified to

$$\mathcal{L}_t(\theta) = -\frac{\beta_t^2}{2\sigma_t^2(1 - \beta_t)(1 - \bar{\alpha}_t)} \|\epsilon - \epsilon_{\theta}(\mathbf{X}_t, \mathbf{Y}, \mathbf{Z}, t)\|_F^2 + C. \quad (14)$$

In the training phase, we set $\sigma_t^2 = \tilde{\beta}_t$, so $C = 0$. Last, we can optimize the ELBO (6) step-by-step along time and in each step we focus on the simple loss function ignoring hyperparameter coefficients as

$$\mathcal{L}_{\text{simple}}(\theta) = \|\epsilon - \epsilon_{\theta}(\mathbf{X}_t, \mathbf{Y}, \mathbf{Z}, t)\|_p^p, \quad (15)$$

where typically $p = 1$ or 2 for using ℓ_1 and ℓ_2 loss. In our experiments, we use ℓ_1 loss and the ablation study about p will be given in the Sec. IV-E.

E. Network Optimization

Next, we construct the conditional denoising network $\epsilon_{\theta}(\cdot)$ using the U-net architecture. Overall, the network is shown in Fig. 2. Inputs of the U-net consists of 4 parts, $\{\mathbf{X}_t, \mathbf{Y}, \mathbf{Z}, t\}$. We have already compute \mathbf{X}_t by (4) in the forward diffusion process. Then we interpolate LrHSI \mathbf{Y} using bicubic method to the same spatial resolution as HrMSI \mathbf{Z} and concatenate

Algorithm 2: Fusion of DDPM-Fus

Input: paired test LrHSI and HrMSI: $(\mathbf{Y}', \mathbf{Z}')$;
the sub-sequence of $\{1, 2, \dots, T\}$ is denoted as $\{\tau_1, \tau_2, \dots, \tau_d = T\}$

- 1 $\mathbf{X}'_T \sim \mathcal{N}(\mathbf{0}, \mathbf{I})$;
- 2 **for** $t = \tau_d, \dots, \tau_1$ **do**
- 3 $\epsilon \sim \mathcal{N}(\mathbf{0}, \mathbf{I})$ if $t > 1$, else $\epsilon = \mathbf{0}$
- 4 Compute the estimated noise by $\epsilon_{\theta}(\mathbf{X}'_t, \mathbf{Y}', \mathbf{Z}', t)$;
- 5 Sample the denoising output \mathbf{X}'_{t-1} from DDIM [35] sampler (18), (19) and (20);
- 6 **end**

it with HrMSI and noisy image along the channel dimension. These data preprocess can be formulated by

$$\mathbf{Y}_{up} = \text{Bicubic}(\mathbf{Y}) \uparrow_{S \times}, \quad (16)$$

$$\mathbf{IN} = [\mathbf{X}_t, \mathbf{Z}, \mathbf{Y}_{up}]. \quad (17)$$

For simplicity, assuming that the spatial resolution of \mathbf{X} is divisible by \mathbf{Y} , $S = W/w = H/h$. $\uparrow_{S \times}$ represents increasing the spatial resolution of LrHSI S times by bicubic interpolation. $[\cdot]$ denotes the concatenation operator. \mathbf{IN} is the data input of the following denoising network. A U-net is used here to implement the denoising process, which consists of several convolutional residual blocks and attention layers. For clarity, the channel numbers of some main feature maps have been marked on the corresponding layers and the forward computation process is illustrated in Fig. 2. Besides, the current time step t is considered as another condition and is input to each residual block in the form of learned embedding vectors, such as the positional embedding in the Transformer [8]. To specify, the training process of the proposed DDPM-Fus is summarized in Algorithm 1.

F. DDPM-Fus with Fast Sampling

Once training is complete, we can obtain fusion results on the test data by implementing the reverse denoising process. Instead of sampling from (5) step-by-step, we get the fused results via another reverse sampler to reduce the fusion time. This sampler was proposed in [35], where a non-Markovian forward process was designed and allowed to skip steps in the implementation of the reverse process, namely denoising diffusion implicit models (DDIM). Specifically, the new forward process can be formulated by

$$\begin{aligned} q_{\sigma}(\mathbf{X}_{t-1}|\mathbf{X}_t, \mathbf{X}_0) \\ = \mathcal{N}(\sqrt{\bar{\alpha}_{t-1}} \mathbf{X}_0 + \sqrt{1 - \bar{\alpha}_{t-1} - \sigma_t^2} \cdot \frac{\mathbf{X}_t - \sqrt{\bar{\alpha}_t} \mathbf{X}_0}{\sqrt{1 - \bar{\alpha}_t}}, \sigma_t^2 \mathbf{I}). \end{aligned} \quad (18)$$

Based on the above relation, we can use the estimated values of \mathbf{X}_0 and noises to implement the reverse process as

$$\mathbf{X}_0 \approx \frac{\mathbf{X}_t - \sqrt{1 - \bar{\alpha}_t} \epsilon_{\theta}(\mathbf{X}_t, \mathbf{Y}, \mathbf{Z}, t)}{\sqrt{\bar{\alpha}_t}}, \quad (19)$$

$$\frac{\mathbf{X}_t - \sqrt{\bar{\alpha}_t} \mathbf{X}_0}{\sqrt{1 - \bar{\alpha}_t}} \approx \epsilon_{\theta}(\mathbf{X}_t, \mathbf{Y}, \mathbf{Z}, t). \quad (20)$$

To specify, we can obtain the fused results on the test data by implementing the reverse denoising process concluded in Algorithm 2.

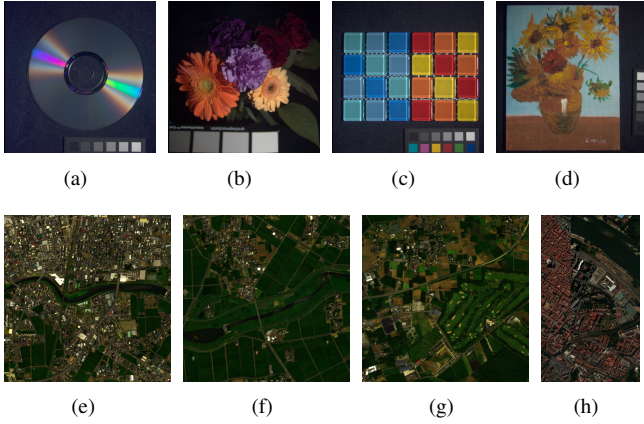


Fig. 3. Some benchmark RGB images in datasets, **CAVE**: (a) *CD*, (b) *flowers*, (c) *glass tiles* and (d) *oil painting*, **Chikusei**: (e) *region2*, (f) *region6* and (g) *region11*, **Pavia Center**: (h) *Pavia Center*.

TABLE II
QUANTITATIVE METRICS OF THE COMPARISON METHODS ON THE 10 TEST IMAGES FROM THE CAVE DATASET. THE BEST RESULTS ARE IN BOLD, WHILE THE SECOND BEST METHODS ARE UNDERLINED.

Methods	PSNR	SAM	ERGAS	SSIM
PANnet	30.68	13.68	1.11	0.864
HSRnet	41.05	<u>7.94</u>	<u>0.41</u>	<u>0.975</u>
SSRnet	41.73	8.17	0.41	<u>0.975</u>
MHFnet	36.46	22.12	1.64	0.951
EDBIN	40.68	8.96	0.48	0.969
DDPM-Fus	43.66	5.69	0.34	0.986
Ideal value	$+\infty$	0	0	1

IV. EXPERIMENTS

We demonstrate the experimental results of our proposed DDPM-Fus conducted on the CAVE [36]¹ dataset and two remote sensing datasets, namely, Chikusei [37]² and Pavia Center³. For a fair comparison, several algorithms of supervised deep learning-based HSI-MSI fusion methods are implemented with their open-source code, including PANnet [27]⁴, HSRnet [29]⁵, SSRnet [30]⁶, MHFnet [31]⁷ and EDBIN [32]⁸.

A. Data Description

The first dataset is CAVE collected by Apogee Alta U260 camera contains 32 scenes of size 512×512 with 31 spectral bands covering a wavelength range of 400 nm to 700 nm at 10 nm steps. Followed by [31] and [29], we set 20 images as training data and the other 12 images as test data. The second database is Chikusei acquired by the Headwall Hyperspec-VNIR-C imaging sensor over Chikusei, Japan. The original

image comprises 128 bands ranging from 363 nm to 1018 nm with a ground sampling distance (GSD) of 2.5 m, and it is 2517×2335 in spatial size. For convenience, we choose 16 non-overlapped subregions from the raw data for the study, each of which has a 512 by 512 size. We set 10 images as training data and other 6 images as test data. The last image we used is acquired by the ROSIS sensor over Pavia, Italy, which contains 1096×715 pixels and 102 bands covering from 430 nm to 860 nm. A 1088×448 sub-image and another 1088×192 region from it are selected as the training data and test data, respectively, for the evaluation. We refer to the above data as the ground truth (GT) of HrHSI to compare the fusion performance. Several benchmark images in these datasets are illustrated in Fig. 3.

Following [23], [29] and [38], we generate the observed LrHSI by directly averaging the 32×32 spatially disjoint blocks in the HrHSI. For the CAVE, Chikusei and Pavia Center datasets, we use the SRF of Nikon D700 camera⁹, LANDSAT-8¹⁰ and an IKONOS-like sensor to simulate the HrMSI via HrHSI, respectively. The HrMSI of the CAVE dataset has three bands that correspond to the red, green, and blue channels, whereas the HrMSI of the other two remote sensing datasets has four bands, one more NIR band than the former.

B. Experimental Setup

1) *Hyperparameter Settings*: The same architecture of the proposed DDPM-Fus is used for fusion three datasets with the diffusion time step T is set to 2000, which is shown in Fig. 2. The hyperparameter sequence $\{\beta_1, \beta_2, \dots, \beta_T\}$ is set to a sequence with uniform growth from 0 to 0.01. The number of training iterations is set to $250k$ and the Adam optimizer [34] is adopted here. In the training phase, we use the cosine annealing learning schedule [39] with the cycle set to $50k$ steps to promote the convergence, where the maximum learning rate is set to 0.0001. We perform the fusion task on one NVIDIA GeForce RTX 3090 GPU with 24GB memory. Due to the memory limitation, we divide the training images into small patches with the size of 64×64 and the batch size is set to 8.

2) *Performance Metrics*: We use the peak signal-to-noise ratio (PSNR), the relative dimensionless global error in synthesis (ERGAS) [40], the spectral angle mapper (SAM), and the structure similarity to quantitatively evaluate the fused results of comparison methods (SSIM) [41]. PSNR is equivalent to the root mean squared error (RMSE). ERGAS is the average relative RMSE of each channel, which can be used to eliminate intensity effects. SAM compares the similarity of spectra in radian units. The structural similarity between the ground truth and the estimated image is measured using the SSIM criterion, which is widely used in image processing. All evaluation criteria are assessed in the 8-bit range, i.e., [0-255].

C. Experiments on the Indoor Dataset

Table II shows the average performance metrics on the CAVE dataset for all comparison models. Overall, PANnet

¹<https://www.cs.columbia.edu/CAVE/databases/multispectral/>

²<http://naotoyokoya.com/Download.html>

³<https://rslab.ut.ac.ir/data>

⁴<https://xueyangfu.github.io/projects/iccv2017.html>

⁵<https://github.com/liangjiandeng/HSRnet>

⁶<https://github.com/hw2hwei/SSRNET>

⁷<https://github.com/XieQi2015/MHF-net>

⁸<https://github.com/wwhappyli/Deep-Blind-Hyperspectral-Image-Fusion>

⁹https://www.maxmax.com/spectral_response.htm

¹⁰<https://landsat.gsfc.nasa.gov/article/preliminary-spectral-response-of-the-operational-land-imager-in-band-band-average-relative-spectral-response>

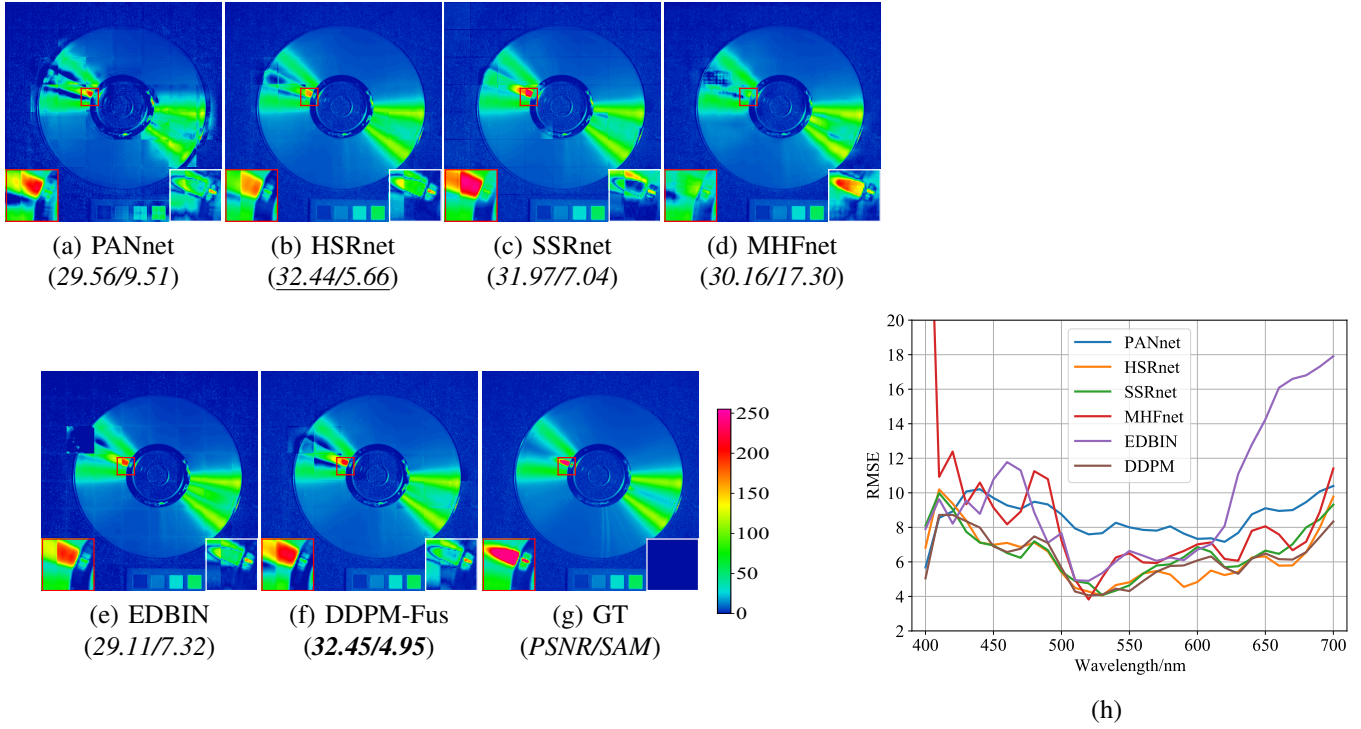


Fig. 4. (a-g) The 21st band (600 nm) of fused HrHSI (CD in the CAVE dataset) obtained by the testing methods, where a ROI zoomed in 9 times (bottom-left) and the corresponding residual maps (bottom-right) are shown for detail visualization. PSNR and SAM are also listed for comparison. (h) The corresponding RMSE along with spectral bands.

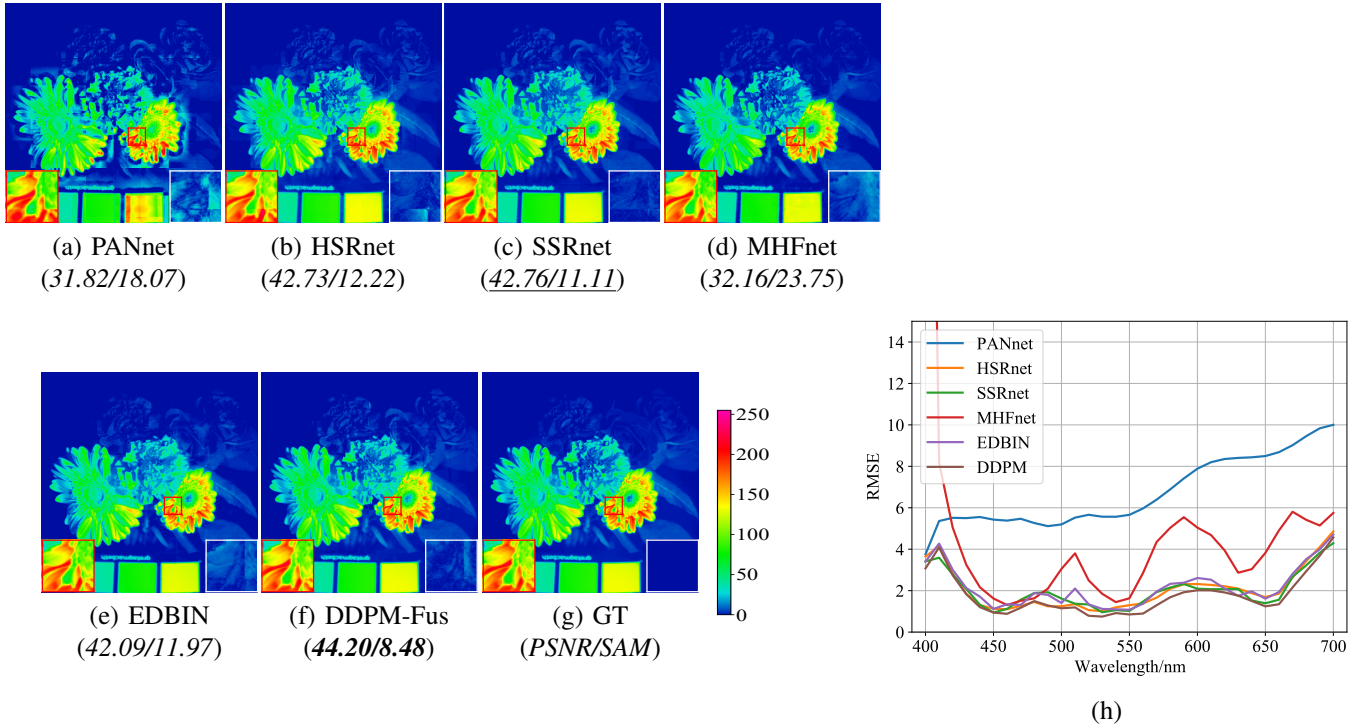


Fig. 5. (a-g) The 21st band (600 nm) of fused HrHSI (flowers in the CAVE dataset) obtained by the testing methods, where a ROI zoomed in 9 times (bottom-left) and the corresponding residual maps (bottom-right) are shown for detail visualization. PSNR and SAM are also listed for comparison. (h) The corresponding RMSE along with spectral bands.

and HSRnet as one-stage fusion methods produce poor results. Compared with them, the multi-stage fusion methods show

competitive performance, especially SSRnet, bringing 0.68 dB improvement in PSNR compared to HSRnet. The existing

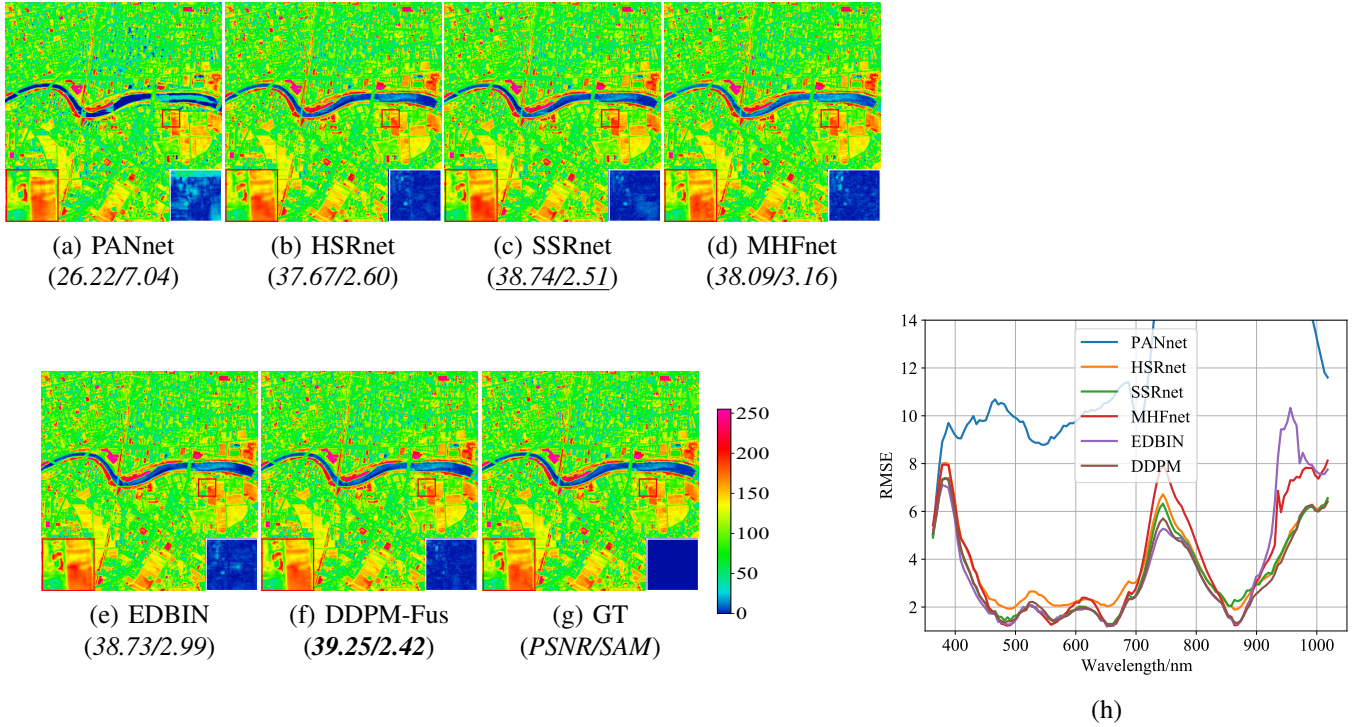


Fig. 6. (a-g) The 73rd band (734 nm) of fused HrHSI (*region2* in the Chikusei dataset) obtained by the testing methods, where a ROI zoomed in 9 times (bottom-left) and the corresponding residual maps (bottom-right) are shown for detail visualization. PSNR and SAM are also listed for comparison. (h) The corresponding RMSE along with spectral bands.

TABLE III
QUANTITATIVE METRICS OF THE COMPARISON METHODS ON THE 6 TEST IMAGES OF THE CHIKUSEI AND THE TEST IMAGE OF THE PAVIA CENTER DATASET. THE BEST RESULTS ARE IN BOLD, WHILE THE SECOND BEST METHODS ARE UNDERLINED.

Methods	Chikusei				Pavia Center			
	PSNR	SAM	ERGAS	SSIM	PSNR	SAM	ERGAS	SSIM
PANnet	28.17	4.31	0.76	0.896	31.63	6.83	0.56	0.940
HSRnet	38.87	2.00	0.42	0.972	44.21	3.37	0.22	0.982
SSRnet	39.66	1.89	0.39	0.974	45.11	2.98	0.19	0.986
MHFnet	39.04	2.33	0.44	0.963	42.82	4.37	0.26	0.977
EDBIN	38.70	2.89	0.43	0.973	<u>45.35</u>	2.93	0.18	0.987
DDPM-Fus	40.25	1.86	<u>0.41</u>	0.975	45.39	3.01	<u>0.19</u>	0.986
Ideal value	$+\infty$	0	0	1	$+\infty$	0	0	1

multi-stage fusion models usually contain several stages, such as coarse fusion, spatial correction and spectral recovery in SSRnet, or scores of fusion steps in MHFnet and EDBIN. Our proposed DDPM-Fus have thousands of fusion stages and we obtain the approximated fused results by the DDIM sampler [35]. Unsurprisingly, the proposed DDPM-Fus outperforms all other fusion models and improves the PSNR by 1.93dB over the second-best model, SSRnet, on the CAVE dataset.

Fig. 4 and Fig. 5 show the fused HrHSI in the 21st band (600 nm) for CD and flowers, respectively. Two regions of interest (ROIs) are highlighted for comparing detailed differences of all testing methods. It can be observed that there are prominent artifacts in the fused image provided by PANnet and EDBIN as shown in Fig. 4 (a) and (e). Besides, the progressive fusion methods, SSRnet and DDPM-Fus, obtain lower error maps than other methods as shown in 5 (c) and (f), respectively.

Clearly, the proposed DDPM-Fus produces the best fusion results of the target HrHSI and corresponding lower absolute error maps than other comparison models. The band-by-band root mean squared error (RMSE) of all methods on these two images are shown in Fig. 4 (h) and Fig. 5 (h) to compare the reconstruction in each band obtained by the testing algorithms. These RMSE results further demonstrate the superiority of our proposed model in spectral reconstruction.

D. Experiments on the Remote Sensing Dataset

We conduct two remote sensing datasets to further evaluate the fusion performance. Remote sensing data, in contrast to indoor images, have lower spatial resolution and typically contain several spectral signatures in a single image. The quantitative metrics of all testing methods over the Chikusei and Pavia Center datasets are shown in Table III. As can

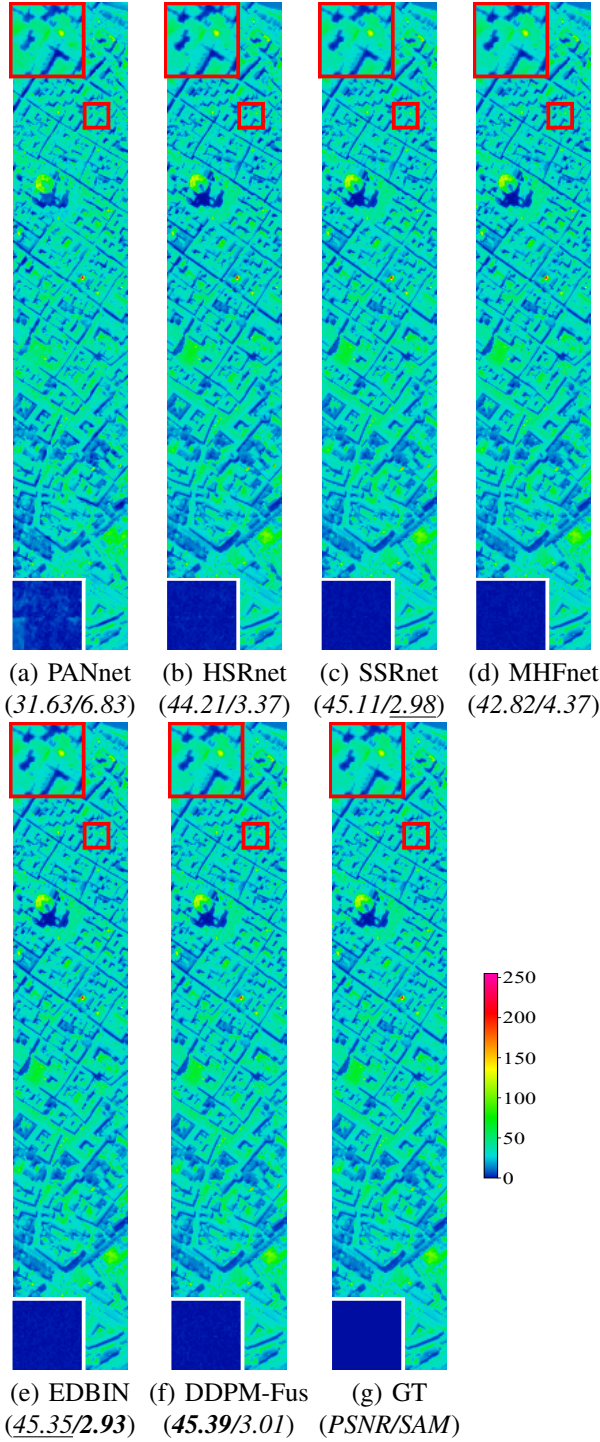


Fig. 7. (a-g) The 31st band (558 nm) of fused HrHSI (*test image* in the Pavia Center dataset) obtained by the testing methods, where a ROI zoomed in 9 times (top-left) and the corresponding residual maps (bottom-left) are shown for detail visualization. PSNR and SAM are also listed for comparison.

be seen, the SAM results tested on these two datasets are significantly smaller than the same metrics evaluated on the CAVE dataset in Table II. Our proposed DDPM-Fus also obtains the best results in terms of the PSNR and is almost optimal in other indicators. In addition, for visual comparison, we present one band in each fused image, as seen in Fig. 6 and Fig. 7. Last, the corresponding RMSE in each band is

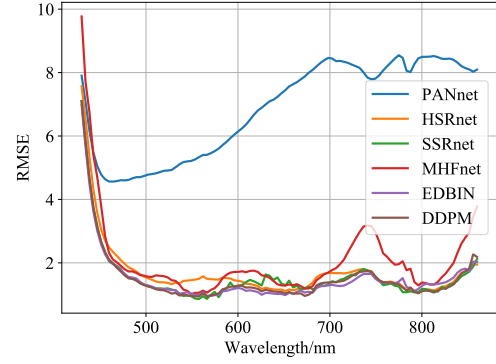


Fig. 8. RMSE along with spectral bands for the comparison methods on the Pavia Center test data.

also shown in Fig. 6 (h) and Fig. 8 and the multi-stage fusion models, such as SSRnet, EDBIN and ours DDPM-Fus are preferred to the one-stage fusion model, PANnet and HSRnet.

E. Model Discussion

1) *Complexity Analysis*: The computational complexity of comparison models heavily depends on the number of parameters and convergence. We list the number of parameters of comparison models, the floating-point operations (FLOPs) when computing one image through each model once and corresponding training time for the three datasets is listed in Table IV. Benefiting from using the DDIM sampler, our proposed DDPM-Fus can achieve the performance of multi-stage fusion models by fusing only once. Meanwhile, as can be seen in Table IV, FLOPs of our model and HSRnet are in the same order of magnitude.

2) *Ablation Study*: We also perform the fusion task with different loss functions and sampling steps to investigate the optimal setting. We implement an experiment conducted on the CAVE dataset and PSNR metrics are shown in Table V. The results show that the ℓ_1 loss is superior to ℓ_2 . Besides, the fusion performance is better when the number of sampling steps in the test phase is set to 1, 2 or 5. Considering the efficiency of the execution, we set the sampling step to 1.

V. CONCLUSION

In this article, we proposed a novel supervised HSI-MSI fusion model based on the conditional denoising diffusion probabilistic model, namely DDPM-Fus. The DDPM-Fus exploit the spatial details and spectral characteristics in the HrHSI via learning the conditional generative model. A U-net is used to learn the noise added in the forward diffusion process. After the DDPM-Fus is trained, the desired HrHSI in the test data can be generated by performing the conditional noise reduction through the reverse process step-by-step. The results of experiments conducted on three publicly available datasets demonstrated the effectiveness and efficiency of our proposed DDPM-Fus. In future research, we will introduce the pre-trained generative diffusion model to enhance the quality of the fused image and develop faster sampling models to reduce fusion time to further improve model efficiency.

TABLE IV
NUMBER OF PARAMETERS, FLOPS AND TRAINING TIME OF COMPARISON MODELS.

CAVE			
	Size ($\times 10^6$)	Flops ($\times 10^9$)	Training time (h)
PANnet	1.08	4.41	3.26
HSRnet	10.24	2.00	2.38
SSRnet	0.03	0.11	1.34
MHFnet	2.16	3.71	5.94
EDBIN	1.24	13.34	34.26
DDPM-Fus	1.69	2.66	11.44

Chikusei			
	Size ($\times 10^6$)	Flops ($\times 10^9$)	Training time (h)
PANnet	16.93	69.33	7.13
HSRnet	156.45	3.05	13.15
SSRnet	0.44	1.81	3.35
MHFnet	29.30	47.72	7.67
EDBIN	18.40	23.19	53.62
DDPM-Fus	1.93	2.72	11.91

Pavia Center			
	Size ($\times 10^6$)	Flops ($\times 10^9$)	Training time (h)
PANnet	10.79	44.18	12.01
HSRnet	100.33	2.70	19.55
SSRnet	0.28	1.15	6.88
MHFnet	19.01	31.00	8.37
EDBIN	11.76	19.88	45.45
DDPM-Fus	1.86	2.70	12.95

TABLE V
PSNR AND FUSION TIME FOR FUSING PER IMAGE WITH DIFFERENT SAMPLING STEPS AND ABLATION STUDY ON LOSS FUNCTIONS CONDUCTED ON THE CAVE DATASET.

Sampling steps	50	20	10	5	2	1
ℓ_1	42.82	43.54	43.68	43.68	43.66	43.66
ℓ_2	37.29	37.49	37.62	37.73	37.75	37.61
Test time (s)	21.25	9.33	5.42	3.75	2.5	1.92

APPENDIX

In this section, we present the derivation of the evidence lower bound (ELBO) (6).

In the DDPM model, all corrupted images, $\mathbf{X}_1, \mathbf{X}_2, \dots, \mathbf{X}_T$, are seen as latent matrices. From the point of variational inference, the true posterior distribution $p(\mathbf{X}_{1:T}|\mathbf{X}_0)$ is approximated by a variational distribution $q(\mathbf{X}_{1:T}|\mathbf{X}_0)$, where $\mathbf{X}_{1:T}$ represents $\mathbf{X}_1, \mathbf{X}_2, \dots, \mathbf{X}_T$ for short. Generally, we minimize the KL divergence between

these two distributions as

$$\begin{aligned}
 & \text{KL}(q(\mathbf{X}_{1:T}|\mathbf{X}_0)||p(\mathbf{X}_{1:T}|\mathbf{X}_0)) \\
 &= \int q(\mathbf{X}_{1:T}|\mathbf{X}_0) \log \frac{q(\mathbf{X}_{1:T}|\mathbf{X}_0)}{p(\mathbf{X}_{1:T}|\mathbf{X}_0)} d\mathbf{X}_{1:T} \\
 &= \int q(\mathbf{X}_{1:T}|\mathbf{X}_0) \log \frac{q(\mathbf{X}_{1:T}|\mathbf{X}_0)p(\mathbf{X}_0)}{p(\mathbf{X}_{0:T})} d\mathbf{X}_{1:T} \\
 &= \int q(\mathbf{X}_{1:T}|\mathbf{X}_0) \log \frac{q(\mathbf{X}_{1:T}|\mathbf{X}_0)}{p(\mathbf{X}_{0:T})} d\mathbf{X}_{1:T} + \log p(\mathbf{X}_0) \\
 &= \log p(\mathbf{X}_0) - \mathbb{E}_q \left[\log \frac{p(\mathbf{X}_{0:T})}{q(\mathbf{X}_{1:T}|\mathbf{X}_0)} \right] \quad (21)
 \end{aligned}$$

Due to the nonnegativity of KL divergence, we get the ELBO of the log-likelihood as

$$\mathbb{E}_q \left[\log \frac{p(\mathbf{X}_{0:T})}{q(\mathbf{X}_{1:T}|\mathbf{X}_0)} \right] \leq \log p(\mathbf{X}_0). \quad (22)$$

Therefore we can maximize the ELBO to achieve the maximum likelihood estimate. Note that the joint distribution of all variables in the forward diffusion and reverse diffusion are

$$q(\mathbf{X}_1, \mathbf{X}_2, \dots, \mathbf{X}_T|\mathbf{X}_0) = \prod_{t=1}^T q(\mathbf{X}_t|\mathbf{X}_{t-1}), \quad (23)$$

$$p(\mathbf{X}_0, \mathbf{X}_1, \mathbf{X}_2, \dots, \mathbf{X}_T) = p(\mathbf{X}_T) \prod_{t=1}^T p_\theta(\mathbf{X}_{t-1}|\mathbf{X}_t). \quad (24)$$

Then, the ELBO can be further simplified as

$$\begin{aligned}
 & \mathbb{E}_q \left[\log \frac{p(\mathbf{X}_{0:T})}{q(\mathbf{X}_{1:T}|\mathbf{X}_0)} \right] \\
 &= \mathbb{E}_q \left[\log p(\mathbf{X}_T) + \log \frac{p(\mathbf{X}_{0:T-1})}{q(\mathbf{X}_{1:T}|\mathbf{X}_0)} \right] \\
 &= \mathbb{E}_q \left[\log p(\mathbf{X}_T) + \sum_{t=1}^T \log \frac{p_\theta(\mathbf{X}_{t-1}|\mathbf{X}_t)}{q(\mathbf{X}_t|\mathbf{X}_{t-1})} \right] \\
 &= \mathbb{E}_q \left[\log p(\mathbf{X}_T) + \sum_{t=1}^T \log \frac{p_\theta(\mathbf{X}_{t-1}|\mathbf{X}_t)}{q(\mathbf{X}_{t-1}|\mathbf{X}_t, \mathbf{X}_0)} \cdot \frac{q(\mathbf{X}_{t-1}|\mathbf{X}_0)}{q(\mathbf{X}_t|\mathbf{X}_0)} \right] \\
 &= \mathbb{E}_q \left[\log \frac{p(\mathbf{X}_T)}{q(\mathbf{X}_T|\mathbf{X}_0)} + \sum_{t=1}^T \log \frac{p_\theta(\mathbf{X}_{t-1}|\mathbf{X}_t)}{q(\mathbf{X}_{t-1}|\mathbf{X}_t, \mathbf{X}_0)} \right] \\
 &= -\text{KL}(q(\mathbf{X}_T|\mathbf{X}_0)||p(\mathbf{X}_T)) \\
 &\quad - \sum_{t=1}^T \text{KL}(q(\mathbf{X}_{t-1}|\mathbf{X}_t, \mathbf{X}_0)||p_\theta(\mathbf{X}_{t-1}|\mathbf{X}_t)). \quad (25)
 \end{aligned}$$

Note that the first term is KL divergence between the distribution of \mathbf{X}_T , the output of the forward diffusion process, and the prior distribution $p(\mathbf{X}_T)$, which is very close to 0 due to the Gaussian diffusion kernel used in the forward process. We ignore the first term, thus, the second term is the desired result (6).

REFERENCES

- [1] Z. Pan, G. Healey, M. Prasad, and B. Tromberg, "Face recognition in hyperspectral images," *IEEE Trans. Pattern Anal. Mach. Intell.*, vol. 25, no. 12, pp. 1552–1560, 2003.
- [2] L. Yan, M. Zhao, X. Wang, Y. Zhang, and J. Chen, "Object detection in hyperspectral images," *IEEE Signal Process. Lett.*, vol. 28, pp. 508–512, 2021.

- [3] J. M. Bioucas-Dias, A. Plaza, G. Camps-Valls, P. Scheunders, N. Nasrabadi, and J. Chanussot, "Hyperspectral remote sensing data analysis and future challenges," *IEEE Geosci. Remote Sens. Mag.*, vol. 1, no. 2, pp. 6–36, 2013.
- [4] K. Zhu, Z. Sun, F. Zhao, T. Yang, Z. Tian, J. Lai, B. Long, and S. Li, "Remotely sensed canopy resistance model for analyzing the stomatal behavior of environmentally-stressed winter wheat," *ISPRS J. Photogramm. Remote Sens.*, vol. 168, pp. 197–207, 2020.
- [5] R. Heylen, M. Parente, and P. Gader, "A review of nonlinear hyperspectral unmixing methods," *IEEE J. Sel. Top. Appl. Earth Obs. Remote Sens.*, vol. 7, no. 6, pp. 1844–1868, 2014.
- [6] N. Yokoya, C. Grohnfeldt, and J. Chanussot, "Hyperspectral and multispectral data fusion: A comparative review of the recent literature," *IEEE Geosci. Remote Sens. Mag.*, vol. 5, no. 2, pp. 29–56, 2017.
- [7] T. Wang, G. Yan, H. Ren, and X. Mu, "Improved methods for spectral calibration of on-orbit imaging spectrometers," *IEEE Trans. Geosci. Remote Sens.*, vol. 48, no. 11, pp. 3924–3931, 2010.
- [8] A. Vaswani, N. Shazeer, N. Parmar, J. Uszkoreit, L. Jones, A. N. Gomez, L. Kaiser, and I. Polosukhin, "Attention is all you need," in *Proc. Annu. Conf. Neural Inf. Process. Syst.*, vol. 30, 2017.
- [9] J. Ho, A. Jain, and P. Abbeel, "Denoising diffusion probabilistic models," in *Adv. Neural Inf. Process. Syst. (NeurIPS)*, vol. 33, 2020, pp. 6840–6851.
- [10] P. Dhariwal and A. Nichol, "Diffusion models beat gans on image synthesis," in *Proc. Annu. Conf. Neural Inf. Process. Syst.*, vol. 34, 2021, pp. 8780–8794.
- [11] N. Chen, Y. Zhang, H. Zen, R. J. Weiss, M. Norouzi, and W. Chan, "Wavegrad: Estimating gradients for waveform generation," in *Proc. Int. Conf. Learn. Represent. (ICLR)*, 2020.
- [12] C. Saharia, J. Ho, W. Chan, T. Salimans, D. J. Fleet, and M. Norouzi, "Image super-resolution via iterative refinement," *IEEE Trans. Pattern Anal. Mach. Intell.*, pp. 1–14, 2022.
- [13] R. Rombach, A. Blattmann, D. Lorenz, P. Esser, and B. Ommer, "High-resolution image synthesis with latent diffusion models," in *Proc. IEEE/CVF Conf. Comput. Vis. Pattern Recognit. (CVPR)*, 2022.
- [14] C. Saharia, W. Chan, H. Chang, C. Lee, J. Ho, T. Salimans, D. Fleet, and M. Norouzi, "Palette: Image-to-image diffusion models," in *ACM SIGGRAPH 2022 Conference Proceedings*, 2022, pp. 1–10.
- [15] L. Loncan, L. B. de Almeida, J. M. Bioucas-Dias, X. Briottet, J. Chanussot, N. Dobigeon, S. Fabre, W. Liao, G. A. Licciardi, M. Simões, J.-Y. Tournier, M. A. Veganzones, G. Vivone, Q. Wei, and N. Yokoya, "Hyperspectral pansharpening: A review," *IEEE Geosci. Remote Sens. Mag.*, vol. 3, no. 3, pp. 27–46, 2015.
- [16] B. Aiazzi, S. Baronti, and M. Selva, "Improving component substitution pansharpening through multivariate regression of MS+Pan data," *IEEE Trans. Geosci. Remote Sens.*, vol. 45, no. 10, pp. 3230–3239, 2007.
- [17] M. Selva, B. Aiazzi, F. Butera, L. Chiarantini, and S. Baronti, "Hypersharpening: A first approach on sim-ga data," *IEEE J. Sel. Topics Appl. Earth Observ. in Remote Sens.*, vol. 8, no. 6, pp. 3008–3024, 2015.
- [18] N. Yokoya, T. Yairi, and A. Iwasaki, "Coupled nonnegative matrix factorization unmixing for hyperspectral and multispectral data fusion," *IEEE Trans. Geosci. Remote Sens.*, vol. 50, no. 2, pp. 528–537, 2012.
- [19] M. Simões, J. Bioucas-Dias, L. B. Almeida, and J. Chanussot, "A convex formulation for hyperspectral image superresolution via subspace-based regularization," *IEEE Trans. Geosci. Remote Sens.*, vol. 53, no. 6, pp. 3373–3388, 2015.
- [20] W. Dong, F. Fu, G. Shi, X. Cao, J. Wu, G. Li, and X. Li, "Hyperspectral image super-resolution via non-negative structured sparse representation," *IEEE Trans. Image Process.*, vol. 25, no. 5, pp. 2337–2352, 2016.
- [21] S. Li, R. Dian, L. Fang, and J. M. Bioucas-Dias, "Fusing hyperspectral and multispectral images via coupled sparse tensor factorization," *IEEE Trans. Image Process.*, vol. 27, no. 8, pp. 4118–4130, 2018.
- [22] Y. Qu, H. Qi, and C. Kwan, "Unsupervised sparse Dirichlet-Net for hyperspectral image super-resolution," in *Proc. IEEE/CVF Conf. Comput. Vis. Pattern Recognit. (CVPR)*, 2018, pp. 2511–2520.
- [23] Z. Wang, B. Chen, H. Zhang, and H. Liu, "Unsupervised hyperspectral and multispectral images fusion based on nonlinear variational probabilistic generative model," *IEEE Trans. Neural Netw. Learn. Syst.*, pp. 1–15, 2020.
- [24] T. Uezato, D. Hong, N. Yokoya, and W. He, "Guided deep decoder: Unsupervised image pair fusion," in *Proceedings of the European Conference on Computer Vision (ECCV)*. Cham: Springer International Publishing, 2020, pp. 87–102.
- [25] V. Lempitsky, A. Vedaldi, and D. Ulyanov, "Deep image prior," in *Proc. IEEE/CVF Conf. Comput. Vis. Pattern Recognit.*, Jun. 2018, p. 9446–9454.
- [26] R. Dian, S. Li, B. Sun, and A. Guo, "Recent advances and new guidelines on hyperspectral and multispectral image fusion," *Information Fusion*, vol. 69, pp. 40–51, 2021.
- [27] J. Yang, X. Fu, Y. Hu, Y. Huang, X. Ding, and J. Paisley, "PanNet: A deep network architecture for pan-sharpening," in *Proc. IEEE Int. Conf. Comput. Vis. (ICCV)*, Oct 2017.
- [28] X. Wang, J. Chen, Q. Wei, and C. Richard, "Hyperspectral image super-resolution via deep prior regularization with parameter estimation," *IEEE Trans. Circuits Syst. Video Technol.*, pp. 1–1, 2021.
- [29] J.-F. Hu, T.-Z. Huang, L.-J. Deng, T.-X. Jiang, G. Vivone, and J. Chanussot, "Hyperspectral image super-resolution via deep spatio-spectral attention convolutional neural networks," *IEEE Trans. Neural Netw. Learn. Syst.*, pp. 1–15, 2021.
- [30] X. Zhang, W. Huang, Q. Wang, and X. Li, "SSR-NET: Spatial-spectral reconstruction network for hyperspectral and multispectral image fusion," *IEEE Trans. Geosci. Remote Sens.*, vol. 59, no. 7, pp. 5953–5965, 2021.
- [31] Q. Xie, M. Zhou, Q. Zhao, D. Meng, W. Zuo, and Z. Xu, "Multispectral and hyperspectral image fusion by MS/HS fusion net," in *Proc. IEEE/CVF Conf. Comput. Vis. Pattern Recognit. (CVPR)*, 2019, p. 1585–1594.
- [32] W. Wang, X. Fu, W. Zeng, L. Sun, R. Zhan, Y. Huang, and X. Ding, "Enhanced deep blind hyperspectral image fusion," *IEEE Trans. Neural Netw. Learn. Syst.*, pp. 1–11, 2021.
- [33] C. Bishop, *Pattern Recognition and Machine Learning*. Springer, January 2006.
- [34] D. P. Kingma and J. Ba, "Adam: A method for stochastic optimization," *arXiv preprint arXiv:1412.6980*, 2014.
- [35] S. Jiaming, M. Chenlin, and E. Stefano, "Denoising diffusion implicit models," in *Proc. Int. Conf. Learn. Represent. (ICLR)*, 2021.
- [36] F. Yasuma, T. Mitsunaga, D. Iso, and S. K. Nayar, "Generalized assorted pixel camera: Postcapture control of resolution, dynamic range, and spectrum," *IEEE Trans. Image Process.*, vol. 19, no. 9, pp. 2241–2253, 2010.
- [37] N. Yokoya and A. Iwasaki, "Airborne hyperspectral data over Chikusei," Space Application Laboratory, University of Tokyo, Japan, Tech. Rep. SAL-2016-05-27, May 2016.
- [38] Z. Wang, B. Chen, R. Lu, H. Zhang, H. Liu, and P. K. Varshney, "Fusion-net: An unsupervised convolutional variational network for hyperspectral and multispectral image fusion," *IEEE Trans. Image Process.*, vol. 29, pp. 7565–7577, 2020.
- [39] I. Loshchilov and F. Hutter, "SGDR: Stochastic gradient descent with warm restarts," in *Proc. Int. Conf. Learn. Represent. (ICLR)*, 2017.
- [40] L. Wald, *Data fusion: definitions and architectures: fusion of images of different spatial resolutions*. Paris, France: Presses des MINES, 2002.
- [41] Z. Wang, A. Bovik, H. Sheikh, and E. Simoncelli, "Image quality assessment: from error visibility to structural similarity," *IEEE Trans. Image Process.*, vol. 13, no. 4, pp. 600–612, 2004.